Strong-Field Modulated Diffraction Effects in the Correlated Electron-Nuclear Motion in Dissociating H_2^+

Feng He,[1,2] Andreas Becker,[2,*] and Uwe Thumm[1]

[1]*James R. Macdonald Laboratory, Kansas State University, Manhattan, Kansas 66506-2604, USA*
[2]*Max-Planck-Institut für Physik of Komplexer Systeme, Nöthnitzer Straße 38, D-01187 Dresden, Germany*

(Received 27 June 2008; published 20 November 2008)

We show that the electronic dynamics in a molecule driven by a strong field is complex and potentially even counterintuitive. As a prototype example, we simulate the interaction of a dissociating H_2^+ molecule with an intense infrared laser pulse. Depending on the laser intensity, the direction of the electron's motion between the two nuclei is found to follow or oppose the classical laser-electric force. We explain the sensitive dependence of the correlated electronic-nuclear motion in terms of the diffracting electronic momentum distribution of the dissociating two-center system. The distribution is dynamically modulated by the nuclear motion and periodically shifted in the oscillating infrared electric field.

DOI: 10.1103/PhysRevLett.101.213002 PACS numbers: 32.80.Rm, 33.80.Rv, 42.50.Hz

The formation and rupture of chemical bonds is determined by the correlated motion of electrons and nuclei on an attosecond time scale. With recent advances in laser technology and the advent of subfemtosecond (fs) laser pulses [1,2], it has become feasible to resolve in time the electronic motion in chemical reactions. This has spurred the investigation of a variety of elementary processes at unprecedented sub-fs time resolution, such as tunnel ionization [3], charge resonance enhanced ionization [4], electron correlation [5,6], electron localization [7], high harmonic generation [8,9], and the emission of core and conduction-band electrons from metal surfaces [10].

Investigation of the electron dynamics in a molecule or a chemical reaction requires the study of the correlated electronic and nuclear motion during the interaction with an ultrashort intense laser pulse. The most elementary molecule H_2^+ and its isotopes are accessible to experimental studies and *ab initio* calculations [11–18]. Its dissociation therefore constitutes an ideal prototype reaction for understanding bound electronic motion during the breakup of chemical bonds in more complex chemical reactions.

Current sub-fs laser technology allows for the control of the final localization of the electron in a dissociating hydrogen molecular ion [7,19–21], which is the first step to understand the control of a chemical reaction in any larger molecule. However, the complex dynamics of the active electron in the time-dependent fields of both nuclei and external laser pulse(s) *before* the electron is localized on one of the nuclei by the rising interatomic barrier is not understood to the best of our knowledge. One may expect that the electron dynamics in the dissociating molecule is an interplay of, at least, field-induced and structural (i.e., interference) effects. Indeed, the mechanism is subtle, and, as we show in this Letter, the expected direction of the electron motion inside the dissociating H_2^+ can follow or oppose the external laser-electric field, depending on the laser intensity.

We study the electronic motion inside H_2^+ molecules by numerically solving the time-dependent Schrödinger equation in three dimensions [13,19,20,22]. In our model, the molecular ion is assumed to remain aligned with the linearly polarized laser pulses. Rotation of the molecule is not included. The interaction of the laser field, given by an external potential $V(t)$, and H_2^+ can be expressed as (we use Hartree atomic units, $e = m = \hbar = 1$ unless indicated otherwise)

$$i\frac{\partial}{\partial t}\Phi(R, z, \rho; t) = [H_0 + V(t)]\Phi(R, z, \rho; t), \qquad (1)$$

with the field-free Hamiltonian

$$H_0 = -\frac{1}{2M}\frac{\partial^2}{\partial R^2} - \frac{1}{2\mu_e}\left(\frac{\partial^2}{\partial z^2} + \frac{\partial^2}{\partial \rho^2} + \frac{1}{\rho}\frac{\partial}{\partial \rho}\right) + \frac{1}{\sqrt{R^2 + \beta}} - \frac{1}{\sqrt{(z - R/2)^2 + \rho^2 + \alpha}} - \frac{1}{\sqrt{(z + R/2)^2 + \rho^2 + \alpha}}. \qquad (2)$$

The reduced masses are $M = 918$ and $\mu_e = 2M/(2M + 1)$, z and ρ designate cylindrical electronic coordinates oriented along the laser polarization, and R is the internuclear distance. The soft-core parameters are $\alpha = 0.0109$ and $\beta = 0.1$ [20,22].

We are interested in the field-driven electron dynamics in the dissociating H_2^+ and launch a dissociating wave packet from the initial $1s\sigma_g$ state onto the $2p\sigma_u$ potential curve in a resonant single-photon transition [20], using a 2-cycle (FWHM) Gaussian attosecond pump pulse. At the end of this UV pump pulse ($t = t_0$), we project Φ onto the $2p\sigma_u$ state, resulting in the projected state $\Phi_{\mathrm{IR}}(R, z, \rho; t_0)$. Subsequently, for $t > t_0$, we propagate Φ_{IR} under the influence of a time-delayed IR pulse. Note that test calculations have shown that the propagation of the full wave function Φ yields the same *final* dissociation probability

and electron localization asymmetry, since the IR pulse does not generate substantial dissociation from the $1s\sigma_g$ state as well as ionization. In the present simulations, the wavelength, peak intensity, and duration of the first UV pulse are 106 nm, 10^{13} W/cm^2, and 0.7 fs, respectively. The wavelength and duration of the IR pulse are fixed at 800 nm and 5.3 fs (2 cycles at FWHM), respectively, while its time delay and intensity are variable. In dipole approximation and in the length gauge, the interaction of the electron with the two pulses is given by

$$V(t) = [E_1(t) + E_2(t - \Delta t)]\left(1 + \frac{1}{1 + 2M}\right)z, \qquad (3)$$

with $E_i(t) = E_{0,i}\exp[-8\ln 2(t/\tau_i)^2]\sin(\omega_i t)$. τ_i are the pulse durations, ω_i the central frequencies, and $E_{0,i}$ the peak electric field amplitudes for the attosecond UV pulse ($i = 1$) and the IR pulse ($i = 2$). Further details of the simulation can be found in [20].

Figure 1 shows the evolution of the dissociation probability $p(z;t) = \int dR \int \rho d\rho |\Phi_{\mathrm{IR}}(R, z, \rho; t)|^2$, integrated over the positive or negative half-space, yielding $P_+(t) = \int_0^{z_{\max}} dz p(z;t)$ and $P_-(t) = \int_{-z_{\max}}^0 dz p(z;t)$, respectively, with $2z_{\max} = 60$ a.u. designating the numerical grid size along the z direction. For all laser intensities, the electron at first oscillates between the two nuclei, as one would expect classically. During the latter part of the laser field, the increasing interatomic barrier eventually blocks the electron transfer between the nuclei [7,20,22], and the electron localization probabilities in the two half-spaces stabilize. Details of the electron motion are strongly intensity-dependent and yield electron localization on opposite centers at different laser peak intensities. For example, the comparison of Figs. 1(b) and 1(c) near 5.5 fs shows that the electron is moving to the (b) negative and (c) positive z axis even though the laser profiles are the same. This surprising result shows that the expected electronic motion does not necessarily follow the direction of the laser field. By increasing the intensity further, to 10^{14} W/cm^2, the electronic transfer dynamics again changes dramatically [Fig. 1(d)].

To gain more insight in the electron motion in the IR-laser field, we Fourier transform the dissociative wave packet along the laser polarization (i.e., in the z direction) and obtain the (partial) momentum representation $\tilde{\Phi}_{\mathrm{IR}}(R, p_z, \rho; t)$. Integration over R and ρ yields the momentum evolution for $t > t_0$

$$P_M(p_z, t) = \int \rho d\rho \int dR |\tilde{\Phi}_{\mathrm{IR}}(R, p_z, \rho; t)|^2 \qquad (4)$$

that is shown in Figs. 2(a)–2(c) for the same intensities as in Figs. 1(b)–1(d). The black dashed line is the momentum of a free electron with zero initial momentum in the IR-laser field: $P_f(t) = -\int^t E_2(t')dt'$.

All panels of Fig. 2 show two main symmetrical momentum streams at the beginning of the IR-laser field and weak side bands at higher momenta. This corresponds to the electron momentum distribution in the initially prepared $2p\sigma_u$ excited orbital, which in terms of a linear combination of atomic orbitals (LCAO) ϕ, can be factorized as $\tilde{\phi}(p_z)\sin(p_z R/2)$, i.e., into an atomic momentum distribution $\tilde{\phi}(p_z)$ and a structure factor $\sin(p_z R/2)$. The interaction with the IR field leads to various degrees of admixture between the $1s\sigma_g$ and $2p\sigma_u$ electronic states of H_2^+. At the lowest and highest intensity, the momentum distribution at large times mainly oscillates with the sin

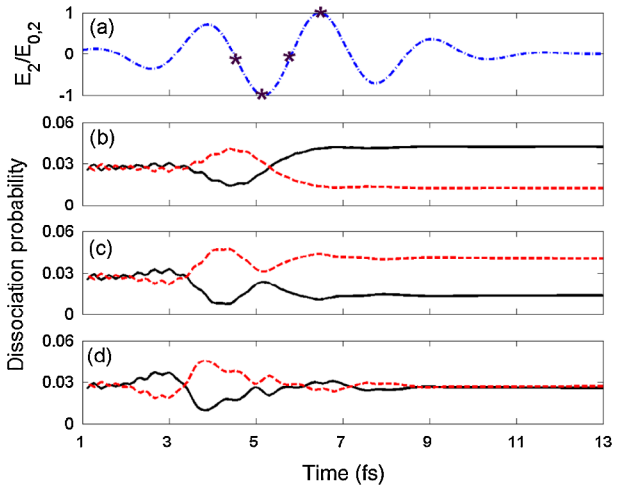

FIG. 1 (color online). Scaled IR laser-electric field for a time delay of 5.8 fs (a). Dissociation probability $P_-(t)$ (solid line) and $P_+(t)$ (dashed line) for the electron to remain in the $z < 0$ and $z > 0$ half-space, respectively, for IR-laser intensities of 3×10^{12} (b), 2×10^{13} (c), and 10^{14} W/cm^2 (d). Stars in (a) correspond to the times selected in Fig. 3.

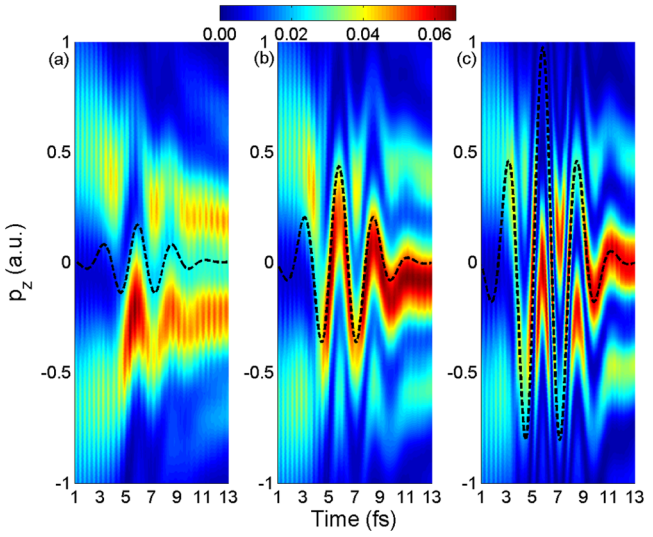

FIG. 2 (color online). Electron momentum distribution P_M along the laser-electric field during the dissociation of H_2^+ in a 5.3 fs IR-laser pulse with a time delay of 5.8 fs and intensities of 3×10^{12} (a), 2×10^{13} (b), and 10^{14} W/cm^2 (c). Dashed lines indicate the classical free-electron momentum in the IR-laser field with zero initial momentum.

[Fig. 2(a)] and cos [Fig. 2(c)] structure factor, indicating that the nuclear wave packet primarily dissociates along diabatic and adiabatic potential curves, respectively. The structure factors generate in p_z oscillating momentum distributions and define sidebands that converge as time (that is, R) increases, clearly pointing to electronic diffraction.

Most interestingly in the present context, for the comparatively low IR-laser intensity in Fig. 2(a), the momentum streams do not change direction (no change in the sign of p_z), while the intermediate intensity in Fig. 2(b) induces larger amplitude oscillations that lead to a change in the direction of the most intense momentum components. This corresponds to the electronic motion observed in Fig. 1(c). At the highest laser intensity in Fig. 2(c), the momentum shift induced by the IR-laser field is large enough to not only change the momentum direction in the main stream but also to pull the sidebands to low momenta. The intensity of these sideband components increases strongly once they reach low momenta. At the same time, the main-band components that closely follow the classical free-electron momentum (dashed curve) get depleted when shifted to higher momenta. The gain in intensity for low momenta is explained based on the LCAO representation of the momentum distributions as due to $\tilde{\phi}(p_z)$, which is strongly enhanced at $p_z = 0$. The extreme momentum shifts of both main and sidebands across the $p_z = 0$ line, together with the intensity gain for low momenta, therefore explain the sub-fs oscillations in the electron motion in Fig. 1(d).

The separate investigation of the electronic dynamics in the dissociating molecular ion in either configuration space (Fig. 1) or momentum representation (Fig. 2) can be enhanced by a phase-space analysis in terms of a Wigner distribution (WD) [23]. In order to represent the electronic motion in the $z - p_z$ cut of the total phase space, we integrate the WD over R and ρ and display

$$W(z, p_z; t) = \frac{1}{\pi} \iint \rho d\rho dR \int_{-\infty}^{\infty} dy \Phi^*(R, z + y, \rho; t) \Phi(R, z - y, \rho; t) \exp(2ip_z y) \quad (5)$$

in Fig. 3 for a sequence of 4 times and the three IR-laser intensities used above (cf. Figs. 1 and 2). The selected times are indicated in Fig. 1(a).

A harmonically oscillating electron would move anticlockwise along an ellipse through phase space. By following the evolution of the WD in the IR field [24], we observe that part of our electron distribution also moves anticlockwise along an approximately elliptical path. Figure 3 shows enhanced intensities near the nuclei at $z = \pm\langle R\rangle/2$. The red spots (positive values) that are centered at $z = 0$ and at discrete momenta that equal integer multiples of $2\pi/\langle R\rangle$ correspond to electronic diffraction peaks. These peaks occur at the reciprocal lattice points of the two nuclei and express the intrinsic two-center interference in H_2^+. The blue spots (negative values) centered at $z = 0$ disappear when the WD is integrated over z (yielding the momentum distribution) yet are physically relevant by defining inaccessible regions in phase space.

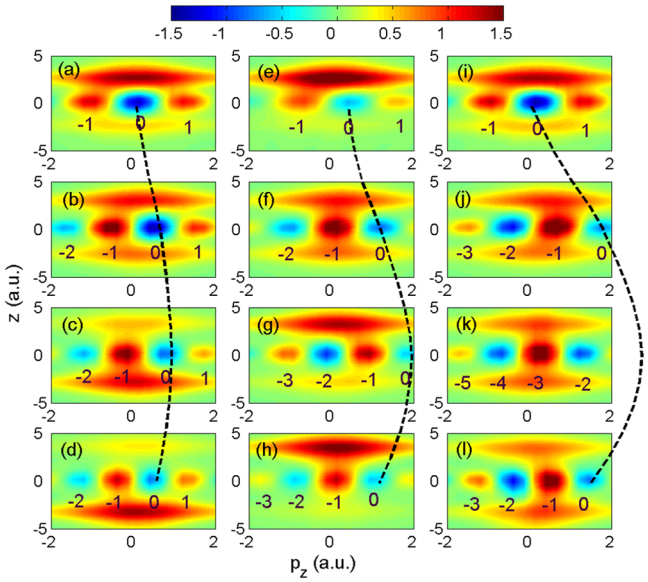

FIG. 3 (color online). Wigner distribution (see text) for IR-laser intensities of 3×10^{12} (left column), 2×10^{13} (middle column), and 10^{14} W/cm^2 (right column) and time delays of 4.5, 5.2, 5.8, and 6.5 fs [in increasing order from the top to the bottom row; cf. stars in Fig. 1(a)]. The dashed lines indicate the oscillations of the momentum gate initially centered at $p_z = 0$.

In order to transfer between the nuclei, the electron is subjected to two-center diffraction constraints that restrict the electronic flux in phase space to cross the $z = 0$ line through one of the "allowed" diffraction momentum spots. These spots therefore act as "momentum gates." We label the field-free gates with positive ($p_z > 0$) and negative ($p_z < 0$) integers. The gate initially centered at $p_z = 0$ is labeled "0."

The momentum gates shift back and forth with the IR-laser period [24], as indicated by the dashed lines in Fig. 3. Their oscillation amplitude depends on the laser intensity. For the small IR intensities (left column), no gate crosses the $p_z = 0$ line during the interaction with the IR pulse. For example, electronic flux that starts with some positive momentum in gate 1 of Fig. 3(a) moves to the nucleus at $z = R/2$ and continues to flow anticlockwise along an approximately elliptical path. Next, this flux passes gate -1 [Fig. 3(b)] and approaches the nucleus at $z = -R/2$ [Fig. 3(c)]. Hereafter, the interatomic barrier has become high enough to block electron transfer, and the electron remains localized near $z = -R/2$ [Fig. 3(d)].

The scenario is different at the intermediate laser intensity (middle column of Fig. 3). The first step in Fig. 3(e) is the same as in Fig. 3(a), except for an increased intensity of the counterclockwise moving electronic flux. Starting with Fig. 3(f), the dynamics is distinctly different from the lower-intensity scenario in the left column: The electronic flux does not continue to move counterclockwise. Instead, it attempts to move toward the nucleus on the negative

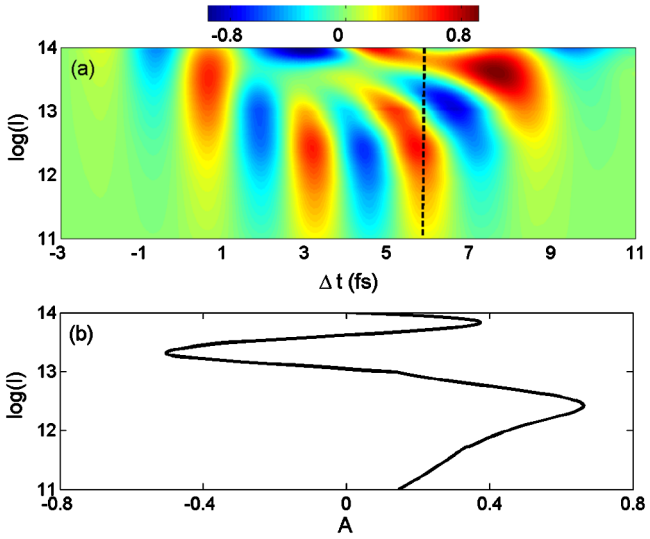

FIG. 4 (color online). (a) The asymmetry parameter as a function of time delay Δt and IR-laser intensity. (b) Cut for the fixed time delay $\Delta t = 5.8$ fs [shown by the dashed line in (a)].

z axis, through gate -1 that is being shifted across the favored $p_z = 0$ region [cf., interpretation of Fig. 2(b) above]. As gate -1 has shifted to positive momenta [Fig. 3(g)], the direction of the electronic flux has reversed before the rising ultrafast potential-barrier shutter disables internuclear electron transfer. This leads to electron localization on the nucleus at $z = R/2$ [Fig. 3(h)], i.e., on the opposite nucleus as in the lower-intensity example in the left column of this figure. At the highest laser intensity of 10^{14} W/cm^2 (right column of Fig. 3), not only gate -1 but also gates -2 and -3 cross the $p_z = 0$ line. This bunching of electric flux leads to the pronounced high frequency oscillations in Fig. 1(d).

In order to quantify the degree of electron localization, we define the asymmetry parameter $A = [P_-(t_f) - P_+(t_f)]/[P_-(t_f) + P_+(t_f)]$, where t_f is the time when the dissociation probability in each nuclear side becomes stable. Figure 4(a) shows A as a function of time delay and IR-laser intensity, while Fig. 4(b) is the cut at $\Delta t = 5.8$ fs. For a fixed intermediate delay, the electronic localization can be controlled very effectively, but not straightforwardly, by tuning the IR intensity. The high amplitude and low-frequency change of A facilitates the experimental control of electron localization even if the laser intensity is not exactly known. We have estimated that a robust control can be achieved for intensity uncertainties up to 10%, which can be realized with current laser technology [16].

In conclusion, depending on the IR-laser intensity, the direction of the electron motion in the dissociating H_2^+ can follow or oppose the IR laser-electric force. Our interpretation of this effect in phase space is based on the passage of electronic flux through diffracting momentum gates that may or may not allow the electron to transfer to the other nucleus. It reveals that the IR-laser field dynamically shifts the gates, causing the electron to explore different gates at different laser intensities. Our results show how the internal electron dynamics in H_2^+ is driven by both the external laser field and the diffraction effects. Looking ahead, we expect that the dynamics and control of electronic motion at a sub-fs time scale in any other molecule should also be affected by at least these two effects. Indeed, diffraction effects have been found to play an important role in the phenomenon of suppressed molecular ionization in fullerenes [25].

This work was supported by the NSF and the Division of Chemical Sciences, Office of Basic Energy Sciences, Office of Energy Research, and U.S. Department of Energy.

*Present address: Department of Physics and JILA, University of Colorado, Boulder 80309-0440, USA.

[1] P. B. Corkum and F. Krausz, Nature Phys. **3**, 381 (2007).
[2] E. Goulielmakis *et al.*, Science **317**, 769 (2007).
[3] M. Uiberacker *et al.*, Nature (London) **446**, 627 (2007).
[4] A. Staudte *et al.*, Phys. Rev. Lett. **98**, 073003 (2007).
[5] A. Staudte *et al.*, Phys. Rev. Lett. **99**, 263002 (2007).
[6] S. X. Hu and L. A. Collins, Phys. Rev. Lett. **96**, 073004 (2006).
[7] M. F. Kling *et al.*, Science **312**, 246 (2006).
[8] H. Xiong *et al.*, Phys. Rev. A **75**, 051802(R) (2007).
[9] P. Lan *et al.*, Phys. Rev. A **76**, 051801(R) (2007).
[10] A. L. Cavalieri *et al.*, Nature (London) **449**, 1029 (2007).
[11] E. Charron, A. Giusti-Suzor, and F. H. Mies, J. Chem. Phys. **103**, 7359 (1995).
[12] G. L. Kamta and A. D. Bandrauk, Phys. Rev. Lett. **94**, 203003 (2005).
[13] S. Chelkowski, A. D. Bandrauk, A. Staudte, and P. B. Corkum, Phys. Rev. A **76**, 013405 (2007).
[14] B. Feuerstein *et al.*, Phys. Rev. Lett. **99**, 153002 (2007).
[15] X. M. Tong and C. D. Lin, Phys. Rev. Lett. **98**, 123002 (2007).
[16] J. McKenna *et al.*, Phys. Rev. Lett. **100**, 133001 (2008).
[17] B. Feuerstein and U. Thumm, Phys. Rev. A **67**, 063408 (2003); U. Thumm, T. Niederhausen, and B. Feuerstein, Phys. Rev. A **77**, 063401 (2008).
[18] S. Pieper and M. Lein, Phys. Rev. A **77**, 041403(R) (2008).
[19] V. Roudnev, B. D. Esry, and I. Ben-Itzhak, Phys. Rev. Lett. **93**, 163601 (2004).
[20] F. He, C. Ruiz, and A. Becker, Phys. Rev. Lett. **99**, 083002 (2007); J. Phys. B **41**, 081003 (2008);Phys. Rev. A (to be published).
[21] S. Gräfe and M. Y. Ivanov, Phys. Rev. Lett. **99**, 163603 (2007).
[22] F. He and A. Becker, J. Phys. B **41**, 074017 (2008).
[23] E. P. Wigner, Phys. Rev. **40**, 749 (1932).
[24] See EPAPS Document No. E-PRLTAO-101-083848 for three movies of the evolution of the Wigner distribution in the infrared laser pulse. For more information on EPAPS, see http://www.aip.org/pubservs/epaps.html.
[25] A. Jaron-Becker, A. Becker, and F. H. M. Faisal, Phys. Rev. Lett. **96**, 143006 (2006).